4 | g-C_3N_4 Based Heterostructure

This chapter voyages through the interfacial charge dynamics across metal-semiconductor/semiconductor-semiconductor heterojunction. Metal-semiconductor junction is further categorized into 0D-2D and 2D-2D configuration to understand the role of surface contact of co-catalyst in the efficiency of the photocatalytic activity using DFT. Co-catalyst decoration/support governs the charge transfer due to workfunction difference, leading to the formation of Ohmic contactSchottky barrier and downward band bending, whereas the presence of surface dipole moment reverses the electric field direction for the ordered-disordered cluster. Thereafter elaborative study on the semiconductor-semiconductor using Hf-based MXene-supported CN is performed to understand the band edge alignment and the charge transfer. Such noteworthy characteristics demonstrate the usefulness of the investigated samples in effective OER/HER and provide a quick overview of the physics at the interface and the significance of the nature of the interaction between the co-catalyst and the photocatalyst.

4.1 0D/2D & 2D/2D Metal-Semiconductor Heterojunction

Techniques reviewed in Chapter-1 and 3, to improve the overall photocatalytic performance of CN include corrugation of pristine-CN [99], stacking of CN-bilayer [9, 100], the addition of cation [101] and anion [102], cation, and anion impurity within CN framework [8, 40, 89, 103, 104], and formation of metal-semiconductor [37–39, 105]/semiconductor-structure [106]. The metal-semiconductor heterojunction is one of these customized materials that have a charge distribution across the interface and produces an interfacial electric field (E_{if}). This E_{if} bends the bands across the interface, providing one side with the capacity to oxidize and the other to reduce charge transfer by creating an Ohmic contact [107] and Schottky barrier [108]. The heterostructures in discussion exhibit "Surface Plasmon Resonance (SPR)" due to the size of the metallic nanoparticles decorating the CN surface. This property enhances the material's photoresponse even further. Due to the significant shift in Φ, the existence of polar bonds within adsorbates produces an internal electric field (E_{int} [109, 110]) in addition to E_{if} [111] across the interface; this E_{int} modulates E_{if}.

As an excellent electrocatalyst that outperformed HER and OER in alkaline media, Co-B-based metallic compounds have recently attracted a lot of attention. They are also being explored as a co-catalyst with a distinct morphology on CN. Amorphous CoB over CN nanosheets [37] results in 360 mV of overpotential for OER with Tafel slope value 94.4 $mVdec^{-1}$ indicating enhanced electrocatalytic capability [37]. While upward band bending ceased electrons from flowing back and aids in the quick separation of photogenerated charge carriers, Guo et al. [39] showed how to form the CoB-CN Schottky junction for the inactivation of Staphylococcus aureus through the generation of reactive oxygen species. With a H_2 evolution rate of 56.86 $\mu mol/h$, the Co_2B decorated CN photocatalyst [105] displayed ordered symmetry in the short range and disordered symmetry in the long range. The ΔG_{H^*} values of -0.242 and -0.345 eV over the Co and B sites,

respectively, are displayed theoretically on the $Co_2B(002)$ slab over CN. The remarkable efficiency of H_2 generation was attributed to the inhibition of $e^- - h^+$ pairs and the SPR effect induced by the high concentration of free carriers. The existing theoretical and experimental data demonstrate the increase in CN's catalytic activity when it has been decorated with various CoB morphologies. On the other hand, our attention has been drawn to the need to perform a systematic computation for 0D/2D and 2D/2D metal-semiconductor heterostructures with different morphology of CoB over CN due to the lack of systematic theoretical study of HER and OER and the role of interface interaction on the charge transfer dynamics within and across the heterojunction.

The current work incorporates a structural analysis over CN to comprehend the electronic, optical, and photocatalytic features of the slab (2D)- and cluster (0D)-CoB. We also investigate the nature of the interaction between such a metal-semiconductor heterostructure, how it affects reaction intermediate adsorption, and how it contributes to OER/HER overpotential.

4.2 CoB-CN Computational Modelling

Using DFT [49, 55, 56] as incorporated in the Quantum Espresso code [76], the structural, electronic, optical, and thermodynamical characteristics of the systems under study have been calculated. The PBE [58] exchange-correlation functional, which is based on the GGA, has been used to execute the structural relaxation. However, for the computation of optical and electronic properties, the HSE06 [60, 61] functional for band gap accuracy has been taken into consideration. 10^{-6} a.u. and 10^{-3} a.u./Å serve as the electronic and force convergence thresholds, respectively, for structural relaxation. The vdW (Grimme-D2 [70]) interaction for total energy correction, the truncation of the Coulomb interaction [112], the vacuum of 25 Å forbidding inter-slab contact, and norm-conserving pseudo-potentials (ONCV) [113] for core correction are taken into consideration. Using a kinetic energy cutoff of 60 Ry for plane wave basis expansion, Monkhorst-Pack k-point grid sampling has been carried out across $6 \times 6 \times 1$ and $3 \times 3 \times 1$, respectively, over the

first Brillouin zone for GGA-PBE and HSE06. Planar unit cells, corrugated unit cells (6.84 Å) [99], and $2 \times 2 \times 1$ supercells (14.24 Å) of CN are used as photocatalysts in our investigation. Distinct morphologies of CoB for the metal co-catalyst include a 2D slab, $(CoB)_2^{2D}$, generated from M_2AlB_2, and two clusters, $(CoB)_2^{0D}$ and $(CoB)_4^{0D}$, of varying sizes, comprising 2Co, 2B and 4Co, 4B, respectively, produced from the orthorhombic phase of CoB are considered. To comprehend the impact of dimensionality and interaction at the interface on the electronic, optical, and overpotential characteristics of HER/OER, three metal-semiconductor heterostructures have been examined, which are $(CoB)_2^{0D}$-CN, $(CoB)_4^{0D}$-CN, and $(CoB)_2^{2D}$-CN. Their respective lattice parameters are 14.24 Å, 14.24 Å, and 6.4 Å. Due to the Co(d_π)-N^{edge}(p_π) interaction, prior research indicates that the CN-void is the best location for Co loading. As a result, the $(CoB)_2^{0D}$-cluster is decorated over the CN triazine mesh. An average lattice parameter within the elastic limits was used to correct for the lattice mismatch in the $(CoB)_2^{2D}$-CN-2D slab model with a hexagonal shape, which was optimized with an interlayer distance of $\approx$ 4.2 Å over CN. Following the formulation by Nørskov et al. [73–75], the reaction kinetics for the evolution of hydrogen and oxygen across all systems are computed. The previous section provides a detailed reaction for the calculation of the adsorption energy (ΔE_{ads}, Eq. 2.42), Gibbs free energy (ΔG, Eq. 2.49), and overpotential ($\eta^{OER/HER}$, Eq. 2.50). The H-atom, H_3O-molecule, and H_2O-molecule have been adsorbed over the heterostructures under consideration, according to the criterion of adsorption site selection [98].

4.3 CoB-CN Structural and Electronic Properties

Fig. 4.2 displays the DOS of $(CoB)_2^{0D}$-CN, $(CoB)_4^{0D}$-CN, and $(CoB)_2^{2D}$-CN, which have band gap values of 1.85, 1.4, and 0.95 eV, respectively. In addition to band gap narrowing relative to pure CN, impurity bands are seen in $(CoB)_2^{0D}$-CN and $(CoB)_2^{2D}$-CN close to the margins of the VB and CB, respectively. A comparative analysis of the TDOS of all three structures reveals that when cluster size increases and dimensionality shifts from 0D to 2D, there is a greater degree

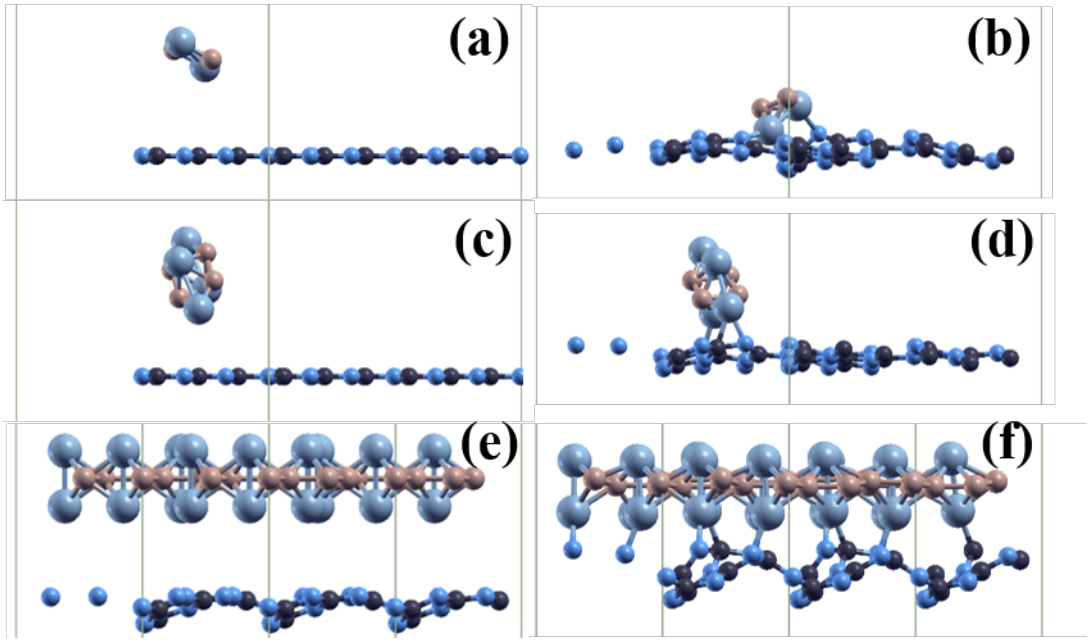

FIGURE 4.1: (a, c, e) Initial, and (b, d, f) optimized structure for $(CoB)_2^{0D}$-CN, $(CoB)_4^{0D}$-CN, and $(CoB)_2^{2D}$-CN.

of delocalization of states. In Fig. 4.2a for $(CoB)_2^{0D}$-CN, the interaction between the lone pair of N^{edge}-atom and the Co-3d orbital results in the formation of a localized impurity state close to the VB edge. In addition to the substantial contributions from N and Co atoms in the VB and C atoms in the CB, the CB, and VB shifting towards E_F suggests a strong hybridization between Co-N and Co-C atoms. The homogeneous distribution of B states on both sides of E_F indicates the B atom's contribution to charge carrier facilitation across the interface. While N/C-2p displays a similar distribution of the state across the energy region, the inclusion of two extra Co/B atoms in $(CoB)_4^{0D}$-CN improves the hybridization of Co-B within cluster geometry, displaying concentrated Co-3d states in the VB of Fig. 4.2b. Narrowed band gap because of the enhanced binding character of the cluster follows the increased states of B-2p in the CB, which indicates increased electronegativity difference between Co-B atoms. The 2D slab structure of $(CoB)_2^{2D}$ contributes a delocalized configuration to the DOS of $(CoB)_2^{2D}$-CN in Fig. 4.2c, while the interaction between Co(3d)-C/N(2p) results in the formation of a partially filled impurity state towards the CB, indicating increased electron concentration on heterostructure formation. Within $(CoB)_4^{0D}$, there is ordered hybridization, and in $(CoB)_4^{0D}$-CN, N^{edge}, B-2p, and Co-3d, B-2p in the

VB and CB, respectively (Fig. 4.2b (ii, iv, v)) suggests the production of impurity level attributing to interface contact. Depending on the dimensionality of CoB, the acceptor and donor levels in $(CoB)_2^{0D}$-CN and $(CoB)_2^{2D}$-CN, respectively, imply the depletion and accumulation of electrons. These impurity levels hence impart different charge transfer trends. This section concludes that because of their strong bonding properties, large nanoparticles do not exhibit variation in electron mobility, whereas evenly dispersed nanoclusters with disordered geometry and long-range ordered geometry across CN do. The ability to reduce the rate of recombination of photo-generated charge carriers results in a higher variance in the curvature of CB/VB edges (compared to CN), a shallow acceptor level, and a deep trap site in $(CoB)_2^{0D}$-CN, $(CoB)_4^{0D}$-CN, and $(CoB)_2^{2D}$-CN, respectively. These features increase the surface reactivity of heterostructures.

Fig. 4.3(a-l) shows the charge density differential ($\Delta\rho$) isosurface for $(CoB)_2^{0D}$-CN, $(CoB)_4^{0D}$-CN, and $(CoB)_2^{2D}$-CN surrounding the cell, respectively, and is represented by (a-d), (e-h), and (i-l). The 0D/2D-metal/semiconductor heterojunction displays cyan-colored charge depletion over Co^{int}-atoms, with semi-localized accumulation and depletion seen for $Co^{non-int} - (CoB)_4^{0D} - CN$. In both situations, there is charge depletion over the N^{edge}-atom and charge accumulation (yellow color) over the C-atom and Co-N/C bond. While charge deposits over the B-B bond and no difference over the B-atom is observed in $(CoB)_4^{0D}$, charge depletion in the form of a lobe is observed in $(CoB)_2^{0D}$. The 2D/2D-metal/semiconductor arrangement exhibits a largely localized and accumulation-dominated isosurface over the Co^{int}-atom, as well as highly localized charge accumulation and depletion over the $Co^{non-int}$-atom. There is an increase of charge over the Co-N bond and surrounding C-atoms, but there is no noticeable change over the B-atom. The study suggests that Co, B, and N electronegativity play a role in enabling the charges within the CN and across the interface, as well as charge redistribution. While the disordered character of $(CoB)_2^{0D}$ attributes to extensive charge redistribution throughout the CN, the periodic and semi-periodic arrangement of $(CoB)_2^{2D}$ and $(CoB)_4^{0D}$ is observable by the charge density difference over B-atom leading to charge distribution over a limited region.

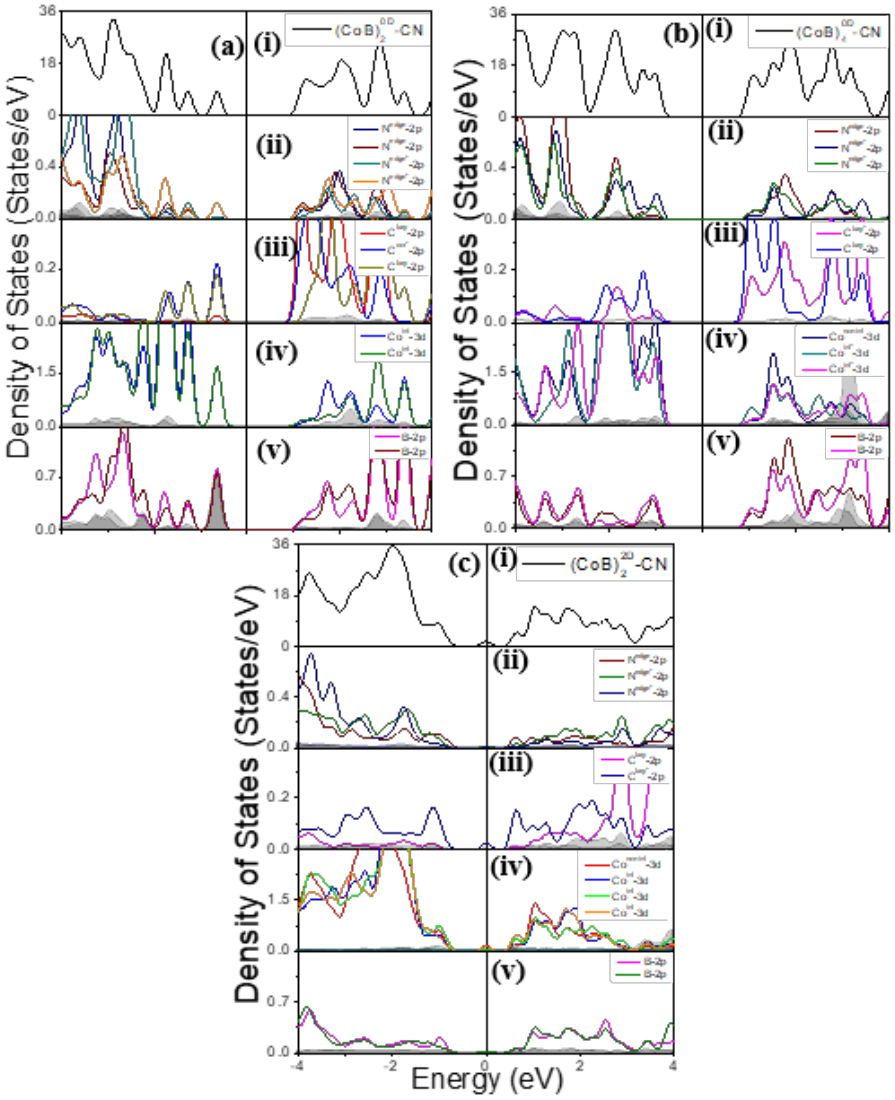

FIGURE 4.2: (a, b, c) Total and (ii-v) partial density of states for $(CoB)_2^{0D}$-CN, $(CoB)_4^{0D}$-CN, and $(CoB)_2^{2D}$-CN with E_F shifted to 0.0 eV, under shaded region is for s-orbitals

In Fig. 4.4(a-c) and (d-f), respectively, the charge distribution and work function difference ($\Delta\Phi$) across the interface are studied using the planar averaged $\Delta\rho$ and the electrostatic potential plot (EPP). To comprehend the change seen from the original structure, EPP of pristine samples are presented in addition to EPP of heterostructures. $(CoB)_2^{0D}$-CN displays charge depletion over $(CoB)_2^{0D}$ and charge accumulation over CN, with cyan and yellow representing charge depletion and accumulation, respectively. Cluster anchoring boosts the charge distribution throughout the semiconductor surface as evidenced by the interface's

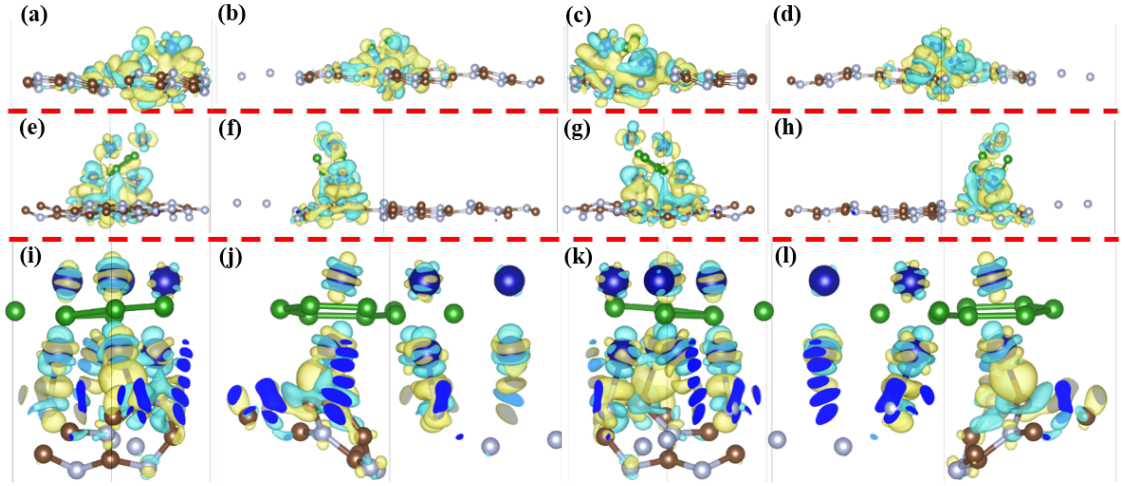

FIGURE 4.3: Charge density difference with charge accumulation and depletion shown by yellow and cyan for (a-d) $(CoB)_2^{0D}$-CN, (e-h) $(CoB)_4^{0D}$-CN, and (i-l) $(CoB)_2^{2D}$-CN.

dominant charge accumulation towards CN and relatively modest charge depletion towards $(CoB)_2^{0D}$. $(CoB)_4^{0D}$-CN exhibits a significant $\Delta\rho$ across the interface, with charge depletion from over Co^{int}-atom and charge accumulation focused over CN. Fig. 4.4c displays the charge distribution over and across the $(CoB)_2^{2D}$-CN interface. It also shows a large $\Delta\rho$ at the interface and an intriguing charge density gradient ($\delta\rho$) across the $(CoB)_2^{2D}$, which is caused by the difference in electronegativity between the Co and B atoms. This $\delta\rho$ rises as the Cobalt boride's periodicity increases; therefore, it is seen for $Co^{non-int} - B$ in $(CoB)_4^{0D}$-CN rather than $Co^{int} - B$ and this is consistent for the 2D/2D-metal/semiconductor heterostructure under study. The $\Delta\Phi$ values for $(CoB)_2^{0D}$-CN, $(CoB)_4^{0D}$-CN, and $(CoB)_2^{2D}$-CN, as seen in Fig. 4.4(d-f), are 0.11, 0.497, and 0.556 eV, respectively, with E_{if} pointing from CN to metal cluster in the former case and E_{if} pointing from metal cluster/slab to CN in the latter two heterostructures. While $(CoB)_2^{0D}$, $(CoB)_2^{0D}$, and pristine planar/corrugated CN do not exhibit any $\Delta\Phi$, $(CoB)_4^{0D}$ (Fig. 4.4e inset) does exhibit a small $\Delta\Phi$, which may be attributed to the synergistic impact of the existence of ordered-disordered geometry.

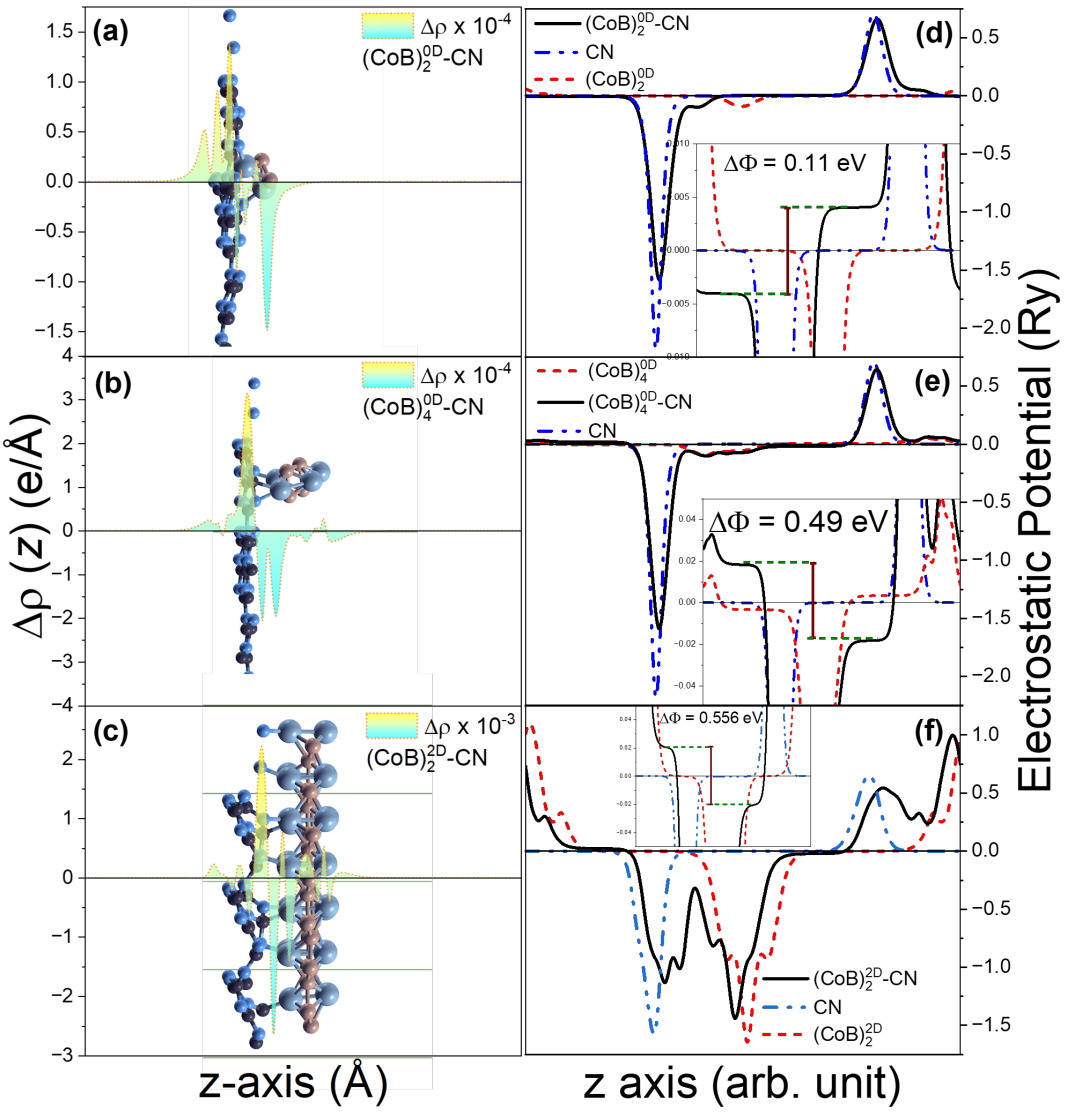

FIGURE 4.4: (a, b, c) Planar averaged charge density difference and, (d, e, f) electrostatic potential profile for $(CoB)_2^{0D}$-CN, $(CoB)_4^{0D}$-CN, and $(CoB)_2^{2D}$-CN, yellow and cyan represent charge accumulation and depletion, inset shows magnified version in small range.

4.4 CoB-CN Optical and Photocatalytic Analysis

The absorbance ($\alpha(\omega)$), which was computed using the frequency-dependent complex dielectric function ($\epsilon(\omega)$), has been used to investigate optical properties. In this case, $\epsilon(\omega)$ yields two parts: ϵ_1, which indicates the degree of polarization, and ϵ_2, which represents dielectric losses. The absorbance curves of all samples are redshifted in Fig. 4.5 as compared to pristine-CN (under shaded region).

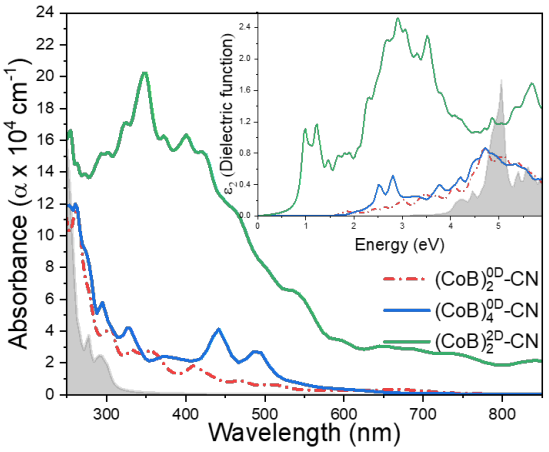

FIGURE 4.5: Absorbance plot for $(CoB)_2^{0D}$-CN, $(CoB)_4^{0D}$-CN, and $(CoB)_2^{2D}$-CN, inset represent imaginary part of dielectric function against photon energy, under shaded region is for gC_3N_4

Increased photogenerated charge carrier is shown by a narrowing of the band gap and an increase in the absorption coefficient determined by an integrating curve in the visible portion of the spectrum. While low-energy optical transitions are observed in heterostructures, high-energy optical transitions are responsible for the light absorption in the high-energy region observed in the ϵ_2 versus Energy plot for CN. Multiple absorption curve spikes in $(CoB)_2^{0D}$-CN and $(CoB)_2^{2D}$-CN indicate multiple transition channels across the forbidden region from the VB to the acceptor level (AL) and the donor level (DL), respectively, as well as to the CB in both instances. The orbital overlap over the interface area is represented by many peaks at lower energy levels, which permit prohibited optical transitions. The peak intensity decreasing from 2D to 0D shows the degree of interfacial orbital coupling.

The band edges that cross the reduction/oxidation potential are what give rise to the photocatalyst's redox potential. With the following VB(CB) values for CN, $(CoB)_2^{0D}$-CN, $(CoB)_4^{0D}$-CN, and $(CoB)_2^{2D}$-CN: 1.66 eV(-1.11 eV), 1.36 eV(-0.49 eV), 0.51 eV(-0.89 eV), and 0.84 eV(-0.11 eV), respectively. $(CoB)_2^{0D}$-CN and CN have effective band edge straddling across redox potential, making them viable options for photocatalytic reduction-oxidation. However, $(CoB)_2^{2D}$-CN, CN, and $(CoB)_2^{0D}$-CN are unable to undergo an oxygen evolution process since

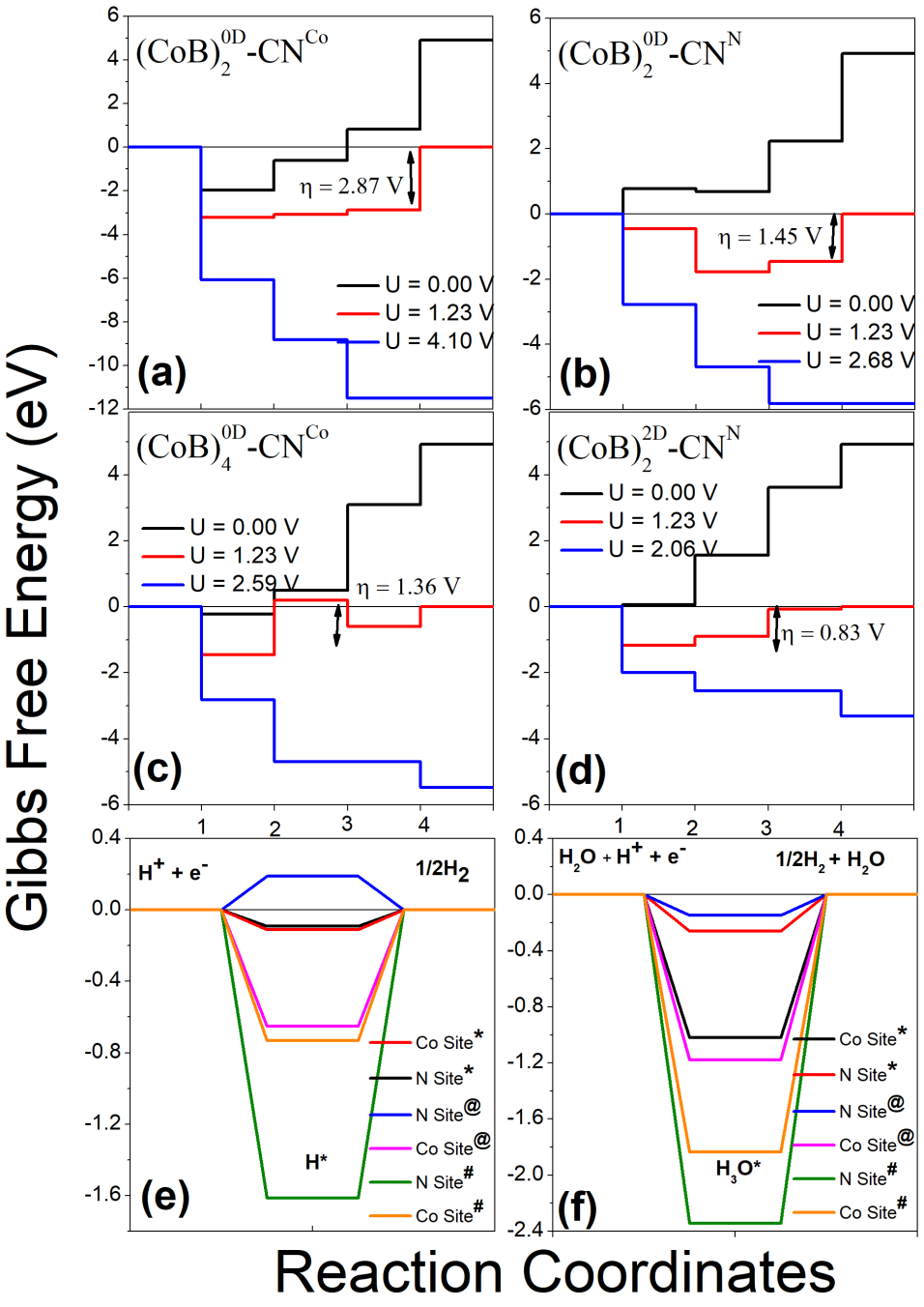

FIGURE 4.6: Gibbs free energy against reaction steps plot (a, b) OER of $(CoB)_2^{0D}$-CN, (c) OER of $(CoB)_4^{0D}$-CN, (d) OER of $(CoB)_2^{2D}$-CN, and (e, f) HER for all systems, * is over $(CoB)_4^{0D}$-CN, # is over $(CoB)_2^{0D}$-CN, @ is over $(CoB)_2^{2D}$-CN

they can only cross the reduction potential and not the oxidation potential.

4.5 CoB-CN Oxygen/Hydrogen Evolution Mechanism

The approach developed by Nørskov and group [73–75] [114] has been used to calculate the reaction η for HER and OER. In this method, a single H-atom or H_3O-molecule is adsorbed across the surface and relaxed to compute the ΔE_{ads}. In contrast, OER involves the successive adsorption of H_2O(Step-1), $OH*$(Step-2), $O*$(Step-3), and $OOH*$(Step-4) before calculating ΔE_{ads} for each reaction intermediate. ΔG [75] is the result of this ΔE_{ads}, pH correction (ΔG_{pH}), zero point energy (ΔZPE), potential (ΔG_U), and entropy change ($T\Delta S$). The reaction barrier for HER and OER is shown by the difference in ΔG & reduction potential and the maximum difference in ΔG of successive reaction intermediates, respectively. $(CoB)_2^{0D}$-CN, $(CoB)_4^{0D}$-CN, and $(CoB)_2^{2D}$-CN exhibit strong physisorption with ΔE_{ads} for H_2O over N(Co)-site of -0.54 eV(-1.09 eV), -0.29 eV(-0.83 eV), and -0.16 eV(-0.86 eV), respectively. The latter two exhibit a moderate physisorption nature over the N-site and all strong chemisorption over the Co-site. While $(CoB)_2^{0D}$-CN can adsorb $OH*$, $O*$, and $OOH*$ across the N/Co-site, $(CoB)_4^{0D}$-CN, and $(CoB)_2^{2D}$-CN can form $OOH*$ only over the N- and Co-sites, respectively therefore OER is not feasible otherwise. As a result, the ΔG plot for a viable reaction only is shown in Fig. 4.6(a, d). OER over $(CoB)_2^{0D}$-CN indicates an energy barrier of 4.10 eV(2.69 eV) over the Co(N)-site for the deprotonation step that results in the creation of O_2. On the other hand, because it requires the addition of an additional water molecule, the rate-determining step for $(CoB)_4^{0D}$-CN(2.57 eV) and $(CoB)_2^{2D}$-CN(2.06 eV) heterostructure is $OOH*$ production. One important factor influencing the change in the OER reaction barrier across the heterostructures [114] under study is the adsorption of water molecules [114].

Its adsorption onto the N/Co atom is dependent upon the E_{if}, charge distribution over the surface, and electronegativity of the reactive site due to the inherent dipole moment of H_2O. In this instance, E_{if} from CN in $(CoB)_2^{0D}$-CN promotes H_2O adsorption in Step-1/3, which helps to raise the reaction barrier for Step-4. However, in $(CoB)_4^{0D}$-CN, $(CoB)_2^{2D}$-CN, the presence of E_{if} provides feasibility for the generation of $OH*$ only if $OOH*$ does not dissociate into $O*, OH*$. If it does not dissociate then the step involving the formation of $OOH*$ is the rate-determining step. $(CoB)_2^{2D}$-CN has the most promising potential for OER at 0.83 V η^{OER}. However, all the samples have the potential to be employed as OER catalysts, with η^{OER} less than prohibited η^{OER} (1.56 V) of CN. Fig. 4.6(e, f) plots the Gibbs free energy change for the H/H_3O over N and the Co-site corresponding to $(CoB)_2^{0D}$-CN, $(CoB)_4^{0D}$-CN, and $(CoB)_2^{2D}$-CN. Value for ΔG for $H(H_3O)$ are -1.62 eV(-2.34 eV), -0.09 eV(-0.26 eV), 0.19 eV(-0.15 eV), and -0.73 eV(-1.84 eV), -0.11 eV(-1.02 eV), -0.65 eV(-1.18 eV) over N and Co, respectively. Because the H-atom exhibits the best adsorption over the N-site in comparison to the Co-site, $(CoB)_4^{0D}$-CN, and $(CoB)_2^{2D}$-CN exhibit lesser adsorption strengths over the N-site, whereas $(CoB)_2^{0D}$-CN exhibits the opposite nature. The E_{if}, from metal cluster/slab to CN in $(CoB)_4^{0D}$-CN, $(CoB)_2^{2D}$-CN, prevents electron transport in the direction of E_{if}, which provides an electron-rich environment that makes the CN layer favorable for the reduction process. $(CoB)_4^{0D}$-CN and $(CoB)_2^{2D}$-CN are most suited for HER due to the nearly zero value of η^{HER} for N-site on H* adsorption.

4.6 CoB-CN Band Bending Analysis

Due to directional charge transfer, uniform cluster distribution over the surface for large reactive sites, and enhanced absorption in visible light, a heterojunction formed with ordered/disordered geometry co-catalyst has synergistically enhanced the photocatalytic efficiency of a semiconductor [115]. Nevertheless, little is known about the charge dynamics within the co-catalyst and at the semiconductor interface. In $(CoB)_2^{0D}$, $(CoB)_4^{0D}$, and $(CoB)_2^{2D}$, the Co(B)-atom

with average charges of -0.496e^-/-0.479e^-(0.386e^-), -0.608e^-/-0.375e^-(0.38e^-), and -0.679e^-/0.694e^-(0.564e^-), respectively, demonstrate electron-donating (accepting) nature. While CN exhibits N(C) accepting (donating) charges, the charge for N varies as a result of its sp^2 and sp^3 hybridization; over planar and corrugated-CN, N/C-atom charge fluctuation is identical. While B and N both accept e^-, with some exceptions, leading in a total electron donation of -0.428e^-, the Co-atom in $(CoB)_2^{0D}$-CN exhibits additional e^- depletion (-0.558e^-/-0.749e^-) and CN accumulates 0.492e^-. In $(CoB)_4^{0D}$-CN Co/B(-0.448e^-), Co^{int}(from -0.375e^- to $-0.675e^-$) shows charge depletion, whereas N-atom along with C-atom in CN accepts total 0.552e^-. Furthermore, among other heterostructures, $(CoB)_2^{2D}$-CN's Co/B-atom exhibits the largest e^- depletion. Similarly, N/C accepts e^-, leading to -0.634e^-(0.789e^-) depletion(accumulation) over $(CoB)_2^{2D}(CN)$, correspondingly. Co/B exhibits e^- donating/accepting capacity for valence electrons in all systems, but it exhibits inconsistency with the N/C-atoms. Changes in dimensionality from 0D to 2D cause an increase in the charge transfer value variation, which illustrates the redistribution of charges inside the CN frame where an inconsistency in the intrinsic character of the N/C-atom facilitates π-conjugation.

The charge transfer affinity from metal to semiconductor to achieve the equilibrium is observed with the $\Phi(= E_{vac} - E_F)$ values of -4.954 eV, -5.574 eV, -4.24 eV, -3.611 eV, -4.209 eV, -4.523 eV, -4.192 eV, and -4.597 eV for planar-, corrugated-CN, $(CoB)_2^{0D}$, $(CoB)_4^{0D}$, $(CoB)_2^{2D}$, $(CoB)_2^{0D}$-CN, $(CoB)_4^{0D}$-CN, and $(CoB)_2^{2D}$-CN. The influence of Φ in the accumulation layer creation on the CN, which results in downward band bending at the metal-semiconductor interface, is verified by the charge transfer. The semiconductor band bending for $(CoB)_2^{0D}$-CN, $(CoB)_4^{0D}$-CN, and $(CoB)_2^{2D}$-CN is seen with the value of extent of band bending (ϕ_{BB}) 0.43 eV, 0.76 eV, and 0.97 eV, respectively, due to the metallic nature of cobalt boride, which prevents its band bending [107]. Given the Φ values, the E_{if} direction for all heterostructures should be from semiconductor to metal, which is consistent with $(CoB)_4^{0D}$-CN and $(CoB)_2^{2D}$-CN's EPP values but not $(CoB)_2^{0D}$-CN's. The reason for this anomaly [109, 110] is the surface

dipole shift for the disordered metallic cluster; even while E_{int} was present in $(CoB)_4^{0D}$, the E_{if} direction was not significantly impacted by the ordered nature. The separation of the $e^- - h^+$ pair will occur in the presence of light, and this e^-s in CB will readily move to the heterostructure interface. The Ohmic contact inside the heterojunction will be crucial and downward band bending with positive workfunction difference between semiconductor and metal will form the Schottky barrier. The migration of photo-electron to the metal cluster/slab will help produce H_2. Ohmic contact will prevent photo-induced holes from traveling to the interface, allowing the photo-charges to be separated spatially, but the low resistance junction will lead to an effective reduction on both sides. Unidirectional charge transfer in the Schottky barrier will form either side good for reduction and other for oxidation. CN will take part in the oxidation reaction by using the photogenerated hole. The charge transfer mechanism is consistent with the current research, which is why the N-site for $(CoB)_2^{2D}$-CN and the Co-site for $(CoB)_2^{0D}$-CN, respectively, exhibit favorable OER and HER activity.

4.7 2D/2D Semiconductor-Semiconductor Heterojunction

In light of Fig. 1.5 (Chapter 1), here extensive review of 2D-2D semiconductor-semiconductor heterostructure is explored. Within a short period, Hafnium-based MXene are showing high efficiency as a supporter to resolve the shortcomings of existing semiconductors. With a band gap value of 1.44 eV, high solar-to-hydrogen and high power conversion efficiency of 17.14%, and 13.84% is seen for 2D vdW MoS_2/Hf_2CO_2 [116]. With a recombination within 1.86 ns, and hole (electron) transfer time of 978 (331) fs, 2D MoS_2/Hf_2CO_2 heterostructure is proposed with high photocatalytic activity [117]. Hf_2CO_2/WS_2 heterostructure forms a type-II semiconductor as an efficient charge separation scheme with charge transfer from Hf_2CO_2 to WS_2 [118]. Heterostructure present high carrier mobility

($\sim 2.2 \times 10^3 cm^2V^{-1}s^{-1}$) with high light absorption ($\sim 6.3 \times 10^5 cm^{-1}$) providing Hf_2CO_2/WS_2 requirement of water splitting [118]. Hf_2CO_2/GaN heterostructure is considered a potential candidate for high photocatalytic activity due to high visible and UV-light along with high electron mobility of $\sim 2.0 \times 10^4 cm^2V^{-1}s^{-1}$. The study conducted on, $PN - Ti_2CO_2$ and $PN - Hf_2CO_2 (PN - Zr_2CO_2)$ [119] shows a red (blue) shift in excitonic peak position from AlN to GaN. The best options for photocatalytic water splitting are $PN - M_2CO_2$ (P = Al, Ga; M = Ti, Zr, Hf) [119] vdW heterostructure, as shown by the computed photocatalytic characteristics. In $BSe - M_2CO_2$ (M = Ti, Zr, Hf) vdW heterostructures, type-II band alignment is reported which prohibits $e^- - h^+$ pairs from recombining. The Hf_2CO_2/MoS_2 heterostructure was examined using DFT-based first-principles computations under biaxial strain, interlayer coupling, and an electric field. A type-I heterojunction is produced by lateral stretching [120], a type-II heterojunction is produced by lateral compression, and it is also influenced by an external electric field. Together, these effects may be used to adjust the Hf_2CO_2/MoS_2 heterostructure for use in optoelectronic, photonic, electronics, and neuromorphic applications. Therefore, the synergistic effect from Hf_2CO_2 and CN can enhance the overall water-splitting potential. Current work focuses on enhancing the photocatalytic activity of Hf_2CO_2/CN using DFT in terms of band gap reduction, enhancement in visible light absorption, charge redistribution, and separation along with the thermodynamical studies of water splitting reactions (HER and OER). The capability of pristine material for a specific reaction, interlayer orbital overlapping, vdW heterostructure, and formation of the internal electric field show promising photocatalytic potential. Electron density is a crucial parameter for photocatalytic activity enhanced by TM-O interaction in Hf_2CO_2 can be applied for increasing the photocatalytic activity by generating more $e^- - h^+$ pair as its first step.

4.8 Hf_2CO_2/CN Computational Parameters

An *ab-initio* based DFT [55, 56] calculations with in-built Kohn Sham formulation for plane wave-based technique as implemented in the Quantum Espresso Package [76] is explored for structural relaxation and computation of HER and OER reaction investigations of Hf_2CO_2/CN. The algorithm uses an ONCV for core correction and a kinetic energy cut-off of 60 Ry. Grimme-D2 [70] dispersion correction is used to characterize vdW interaction. In addition, a 30 Å vacuum space is considered to avoid periodic inter-slab contact in the z-direction. The Coulomb interaction in the z-direction was truncated to keep the computational parameter similar to our earlier study. All the structures are relaxed to an electronic convergence threshold of 10^{-6} a.u. Maximum force per atom is less than 10^{-3} $a.u./$ Å. The PBE-GGA is considered for atomic position relaxation with a k point grid of $5 \times 5 \times 2$. Electronic properties including DOS, electron localization function (ELF), and electrostatic potential profiles are computed using a self-consistent field cycle. Besides GGA, the hybrid functional HSE06 [60, 61] from the Wannier90 package [68, 69] is considered for accurate band gap estimation at $3 \times 3 \times 3$ k-point mesh. The band structure calculation procedure, which makes use of maximally localized Wannier functions (MLWF), is then followed.

4.9 Hf_2CO_2/CN Structural and Electronic Properties

Based on the availability and suitability of semiconductor-MXene [121] we have explored Hf-based MXene with oxygen termination along with well-known photocatalyst CN. Band gap values of CN and Hf_2CO_2 (HCO) have been calculated within their lattice parameter as 2.87 and 1.63 eV, respectively as also reported earlier [9, 118, 122]. The lattice parameters of 7.122, 6.543 Å for CN, HCO, respectively show a lattice mismatch of $\sim 8\%$, while with ~ 3.75 interlayer distance, vdW correction [70] and ~ 30 vacuum in $z-axis$ the structure was relaxed. This

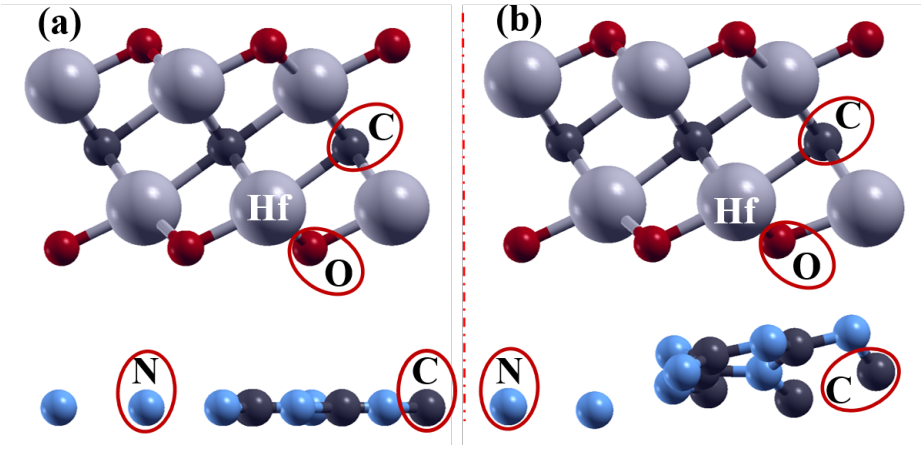

FIGURE 4.7: Initial and optimized structure of the Hf_2CO_2/CN heterostructure

optimized structure in Fig. 4.7 shows $\sim$ 6.627 lattice parameter with a band gap of 1.26 eV for Hf_2CO_2/CN.

band gap correction was performed using hybrid functional, while the value has been calculated using band structure plotted using MLWF. An indirect band gap for CN from $\Gamma \rightarrow K$ on the Brillion zone and direct band gap for HCO from $\Gamma \rightarrow \Gamma$ lead to a direct band gap from $\Gamma \rightarrow \Gamma$ for Hf_2CO_2/CN. Fig. 4.8(a-c) show the band structure and DOS for pristine and heterostructure systems, from Fig. 4.10(a, b) well-defined localized states of C, N-atoms can be seen denoting uniform electron sharing between the $p_\pi - p_\pi$ bonding of C and N. The band structure shows a flat band for the VB denoting heavy holes and large curvature of the CB for rapid electron mobility.

MXene system, based on its synthesis method is terminated with various groups such as O-, F- and OH-, in this quest to find a semiconductor MXene oxygen terminated Hf_2C has been considered and the termination group at various positions were placed, and checked for its energetic stability. The electronic property computation shows curved bands for VB and CB which denote high mobility of the holes and electrons, respectively. This brings the variance of the effective mass to unity leading to a high rate of recombination of the charge carriers. The DOS and PDOS analysis from Figs. 4.8, 4.9(a, b) indicates electron localization within

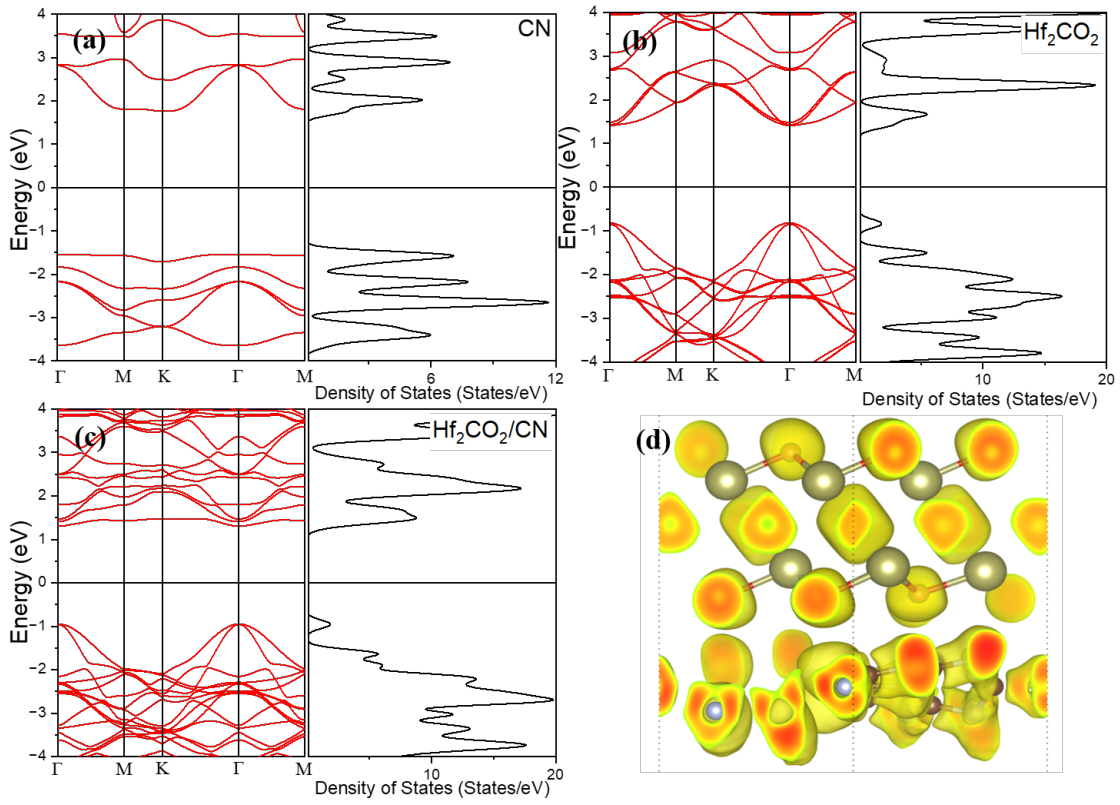

FIGURE 4.8: Band and Density of States for (a) CN, (b) Hf_2CO_2, and (c) Hf_2CO_2/CN, (d) ELF for Hf_2CO_2/CN heterostructure.

the surface and normal to the surface highlighting the O-Hf $p_\pi - d_\pi$ hybridization along with Hf-C $d_\pi - p_\pi$ interaction. The uniform feature for both the upper/lower face O and Hf (denoted by ${}^{U}O/O_L$ and ${}^{U}Hf/Hf_L$) directs towards consistent orbital nature on either side of the 2D slab. A direct band gap within the visible region of the spectrum makes it perfect for the absorbance of yellow light.

The dominance of VB by N^{edge}-2p, Hf-5d, and C^{HCO}-2p is observed along with contribution of Hf-5d, O, C, and N^{tri}-2p in CB, indicating the potential of reduction and oxidation over either surface of the heterostructure. These states on heterojunction formation escape the uniform nature as was seen for pristine material, implying the activation of orbital interaction. Similar findings for the heterostructure have been observed, as the flat band at frontier orbital is dominated by the C/N-atom leading to a reduction of the electron mobility. On the other hand, the

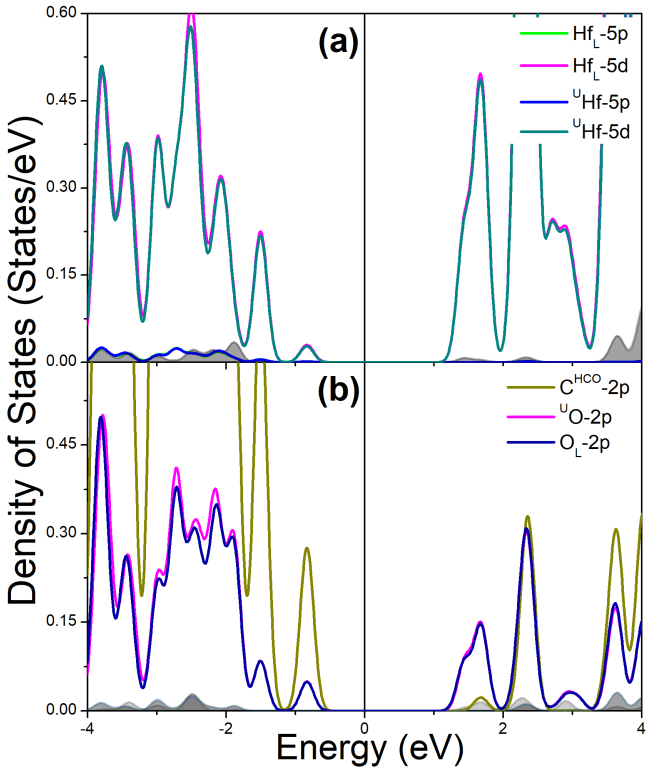

FIGURE 4.9: Partial Density of States for (a) Hf-5p/5d, (b) O/C-2p for Hf_2CO_2.

VB curvature further increases (compared to its pristine counterpart) resulting in rapid hole migration capability. This further increases the variance hence, the recombination rate is further reduced showcasing higher efficiency for photocatalytic reaction. This property is governed by the availability of photogenerated charge carriers on the surface with a large lifetime for higher activity. Suppression and narrowing of the peak as observed from Fig. 4.10 at the VB along with low localization of states directs us towards the planar π-conjugation for each surface and interlayer orbital interaction. Further analysis using the ELF for Hf_2CO_2/CN from Fig. 4.8 verifies the former results presented for the structural and electronic property, ELF plot shows localized state disturbance for the interfacial C-Hf-O interaction, while the isosurface at the other side is consistent in shape. ELF also differentiates between the orbitals at the interface of Hf_2CO_2/void-CN and Hf_2CO_2/mesh-$CN$where the corrugation in the later part is higher due to large orbital interaction between the O and N lone pairs. [123]

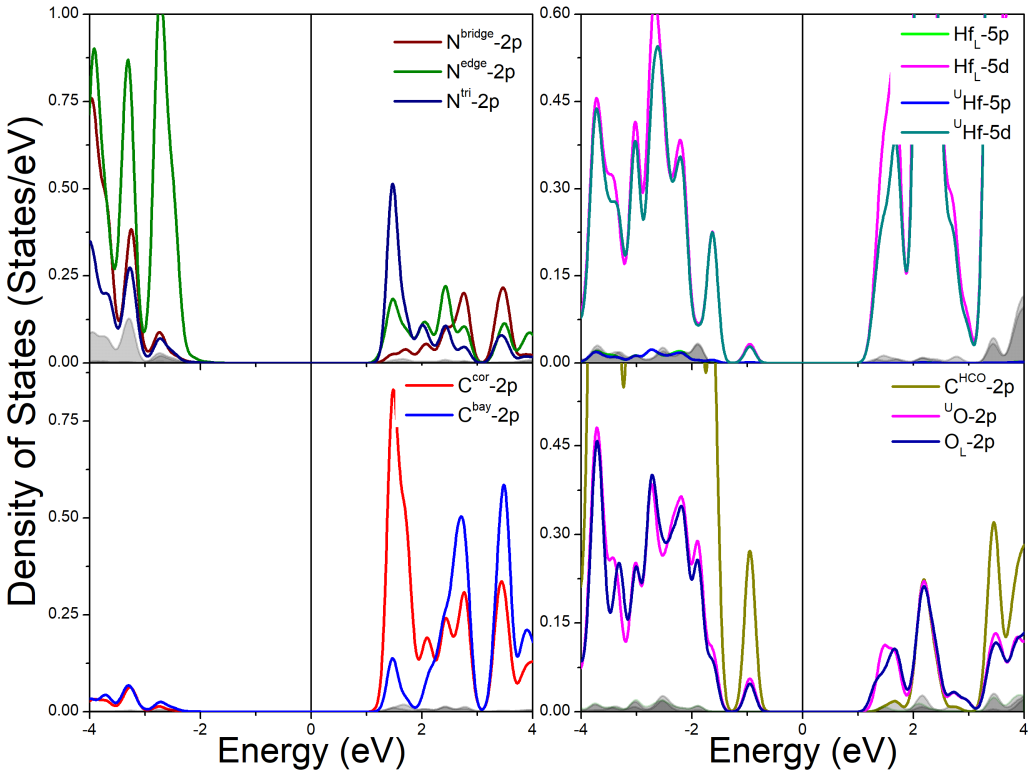

FIGURE 4.10: Partial Density of States for (a) N-2p, (b) C-2p, (c) Hf-5p/5d, (d) O/C-2p (Hf_2CO_2) for Hf_2CO_2/CN heterostructure.

In Fig. 4.11, we see an EPP for pristine and heterostructure. Since the single-layer materials have different potentials and on contact charge transfer channel is being created thus forming a built-in electric field at the interface. This electric field generation contributes to solving the problem of radiative recombination of carriers. EPP has been shifted to zero for clear understanding although, 1.376, 6.759, and 7.982 eV E_{vac} and 2.667, 3.207, and 5.970 eV of Φ value for CN, Hf_2CO_2, and Hf_2CO_2/CN is calculated denoting charge transfer channel formation. The computed charge density difference isosurface and planer average plot across z-the direction in Fig. 4.11b justify the Φ values, here the magenta and cyan areas represent electron accumulation and depletion. The built-in electric field formed in the vdW gap of these heterostructure restraint recombination of photogenerated $e^- - h^+$ pairs. We see that as a result of band bending and interfacial region in the heterostructure, the charge transfer is much more

complicated.

4.10 Hf_2CO_2/CN Optical and Photocatalytic Analysis

Absorbance, the imaginary part of dielectric function and band edges are shown in Fig. 4.11(c, d), where curve shifting in the visible region and absorbance increase are visible. The shaded region is denoted by CN, while the interlayer orbital coupling shows its signature clustering in the absorbance around 450 nm and around 2.8 eV in the dielectric function enhancing the absorbance despite the increase in band gap. The band edges denote reduction-oxidation potential straddling for all the systems studied, The presence of CN imparts higher reduction capability to the heterostructure which was absent in the Hf_2CO_2 system, thus providing larger reduction potential for H_2 production and CO_2 reduction.

4.11 Hf_2CO_2/CN Reduction-Oxidation Mechanism

Along with band gap in the visible region, high charge carrier mobility, low recombination rate, high absorbance for large photo generation of the carrier, and band edges straddling the reduction-oxidation potential, a photocatalyst is required to have an overpotential for OER/HER within the reduction-oxidation potential, respectively. For this, we have simulated the OER/HER on pristine as well as both faces of the heterostructure and the free energy plot has been shown in Fig. 4.12(a-d). With a high overpotential for OER (η^{OER}) of 2.32 V for CN, it was advised to functionalize it to enhance its reaction feasibility. Hf_2CO_2 on the other hand show η^{OER} of 1.16 V and on the formation of Hf_2CO_2/CN we

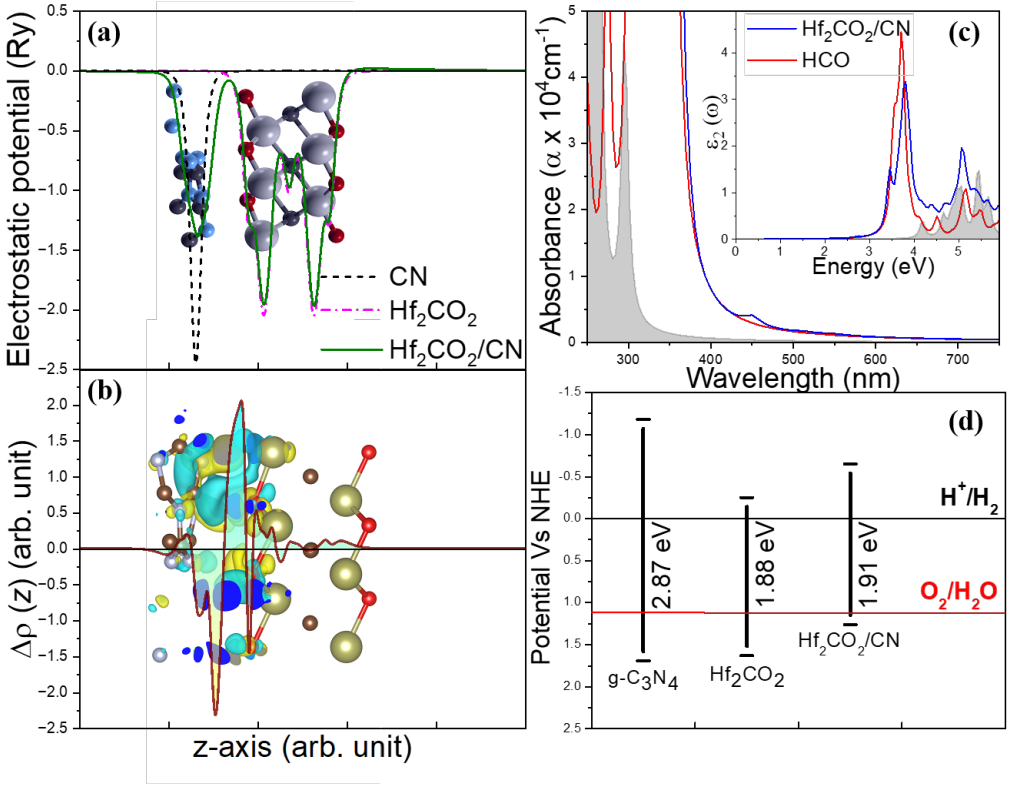

FIGURE 4.11: (a) Electrostatic potential profile, (b) Plane-averaged charge density difference of heterostructure along z-direction normal to the heterostructure. The 3D isosurface is the charge density difference where magenta and cyan areas represent electron accumulation and depletion, respectively, (c) Absorption coefficient: inset(imaginary part of dielectric function), and (d) band edges position of pristine and heterostructure.

see that OER performed over lower(CN side)/upper(Hf_2CO_2 side) Hf_2CO_2/CN (Hf_2CO_2/CN_L/$^UHf_2CO_2/CN$) showed 2.17/1.25 V of η^{OER}. It was seen that the η^{OER} reduced by $\sim$ 2 times for the $^UHf_2CO_2/CN$ denoting Hf_2CO_2 face capable for enhanced OER.

While the overpotential for HER (η^{HER}) derived from the adsorption energy is plotted in Fig. 4.12(e, f), where CN and Hf_2CO_2 for H-atom/H_3O-molecule shows 0.68/1.27 and 1.01/0.39 V indicating the feasibility of HER over Hf_2CO_2 due to the presence of O-termination. While after contact we see η^{HER} for Hf_2CO_2/CN_L and $^UHf_2CO_2/CN$ H-atom/H_3O-molecule to be 0.41/0.33 V and 2.71/3.12 V denoting that CN act as an active surface for HER. The η^{HER} for heterostructure for CN-side is reduced by 50% from Hf_2CO_2 for H-atom case.

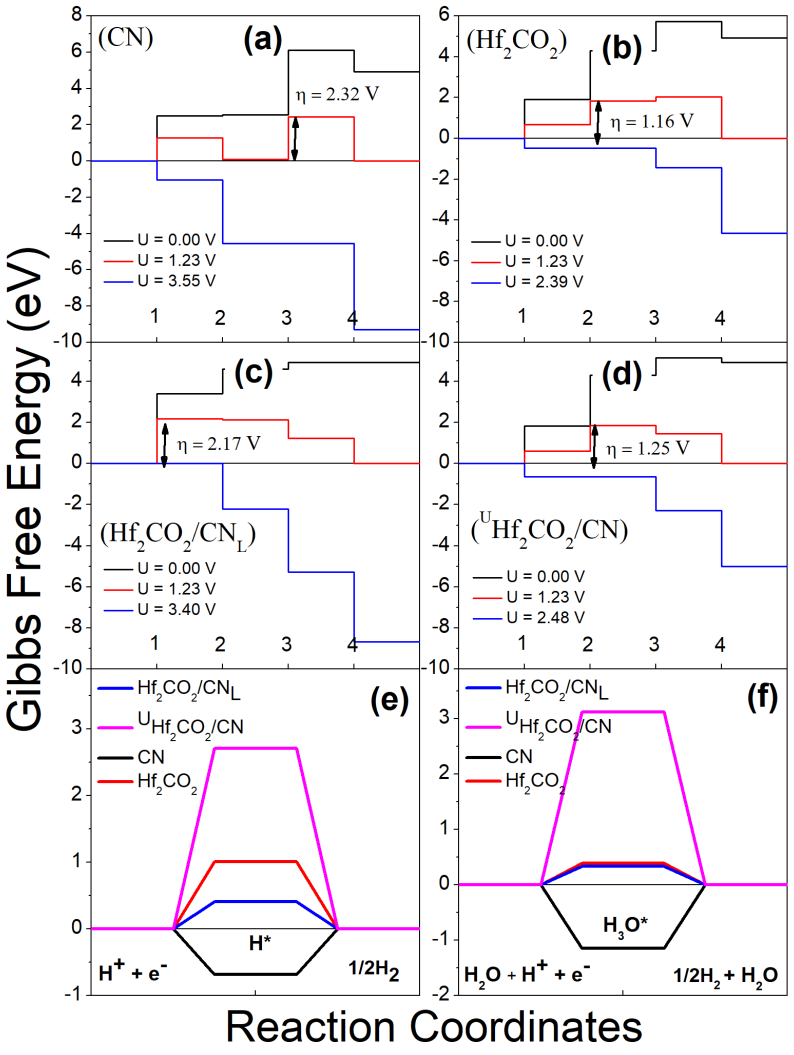

FIGURE 4.12: Gibbs free energy profile for (a) CN, (b) Hf_2CO_2, intermediate adsorbed over Hf_2CO_2/CN over (c) lower, and (d) upper surface for oxygen evolution reaction and (e) H-atom, (f) H_3O, intermediate for hydrogen evolution reaction.

Along with the band edge value straddling and low $\eta^{HER/OER}$ as compared to the pristine case, we can say that the formation of a built-in electric field, charge distribution over the surface and charge transfer vertical to the heterostructure has enhanced the optical absorbance and made the reaction feasible and this material could be used as photocatalyst for HER but and external potential $\sim$ 1.23 V will be required for OER to fall in photocatalysis.

The Φ value governs the electron transfer channel across the interface, here with a smaller value of Φ for CN and larger for Hf_2CO_2 corresponding to the charge transfer from CN to Hf_2CO_2, also verified from the Löwdin charge analysis. This

charge transfer of light illumination will make the Hf_2CO_2 electron-rich and CN hole-rich, thereby generating an electric field from CN to Hf_2CO_2. This charge transfer rich character on the adsorption of the reaction intermediates activates the adsorbate for feasible reaction over the surface which is reflected in the overpotential value of the OER/HER. The lower overpotential over the CN for HER and over Hf_2CO_2 for OER verify the electron reversal prohibition and enhancement of respective photocatalytic activity over either of the faces of the heterostructure.

4.12 Conclusion

The $CoB-CN$ based 0D/2D-2D metal-semiconductor heterostructure is systematically studied to comprehend the optical behavior, charge dynamics, and impact of dimensionality variation on the η of OER/HER. The investigated heterostructures have attained several necessary conditions for an effective photocatalyst, including large reactive sites, low reaction barrier, charge carrier separation with low recombination rate, and high optical absorbance in the visible range. Observations of forbidden migration of holes from semiconductor to metal and production of a charge accumulation layer at the interface have been linked to the formation of downward band bending, E_{if}, E_{int}, and surface dipole generation. The emergence of an ohmic contact gives rise to a reduction and oxidation potential on the semiconductor and metal surfaces, respectively. To understand further the interaction between semiconductor-semiconductor heterostructure, we have studied the Hf_2CO_2/CN, where Hf-based MXene is supported by the CN-photocatalyst. This study provided us with the band bending across the junction along with the formation of the electric field. The unidirectional charge transfer imparts each semiconductor layer with the efficiency of reduction/oxidation reaction. Thus simultaneous HER and OER can take place on either side of the heterostructure. The interlayer orbital interaction was displayed from the ELF plot, along with the narrowing of the band gap leading to large photoinduced charge carrier generation capability. The rapid migration, reduced recombination, and spatial separation

were presented based on effective mass ratio/band curvature describing the potential application of Hf_2CO_2/CN heterostructure as an efficient water-splitting photocatalyst.